Anisotropy in the Raman scattering of a CaFeO 2.5 single crystal and its link with oxygen ordering in Brownmillerite frameworks

ARTICLE *in* JOURNAL OF PHYSICS CONDENSED MATTER · MAY 2015

Impact Factor: 2.35 · DOI: 10.1088/0953-8984/27/22/225403

Anisotropy in the Raman scattering of a $CaFeO_{2.5}$ single crystal and its link with oxygen ordering in Brownmillerite frameworks

2015 J. Phys.: Condens. Matter 27 225403

(http://iopscience.iop.org/0953-8984/27/22/225403)

IOP Publishing Journal of Physics: Condensed Matter
J. Phys.: Condens. Matter **27** (2015) 225403 (11pp) doi:10.1088/0953-8984/27/22/225403

Anisotropy in the Raman scattering of a $CaFeO_{2.5}$ single crystal and its link with oxygen ordering in Brownmillerite frameworks

Andrea Piovano[1], Monica Ceretti[2], Mark R Johnson[1], Giovanni Agostini[3], Werner Paulus[2] and Carlo Lamberti[4,5]

[1] Institut Laue-Langevin (ILL), 71 avenue des Martyrs, 38000 Grenoble, France
[2] University of Montpellier 2, UMR 5253, ICGM, C2M, CC1504, 5 Place Eugène Batallion, 34095 Montpellier, France
[3] European Synchrotron Radiation Facility (ESRF), 71 avenue des Martyrs, 38000 Grenoble, France
[4] Department of Chemistry, NIS Center of Excellence, CrisDi center for crystallography and INSTM unit, University of Turin, Via Giuria 7, I-10125, Turin, Italy
[5] Southern Federal University, Zorge street 5, 344090 Rostov-on-Don, Russia

E-mail: piovano@ill.fr

Received 10 November 2014, revised 23 February 2015
Accepted for publication 7 April 2015
Published 19 May 2015

Abstract

Periodic DFT calculations allow an understanding of the strong orientation-dependent Raman spectra of oriented $CaFeO_{2.5}$ single crystals. Modes involving the oscillation of the apical oxygen (O_{ap}) atoms perturb the induced electric dipoles. These are formed by anisotropy in the charge distribution and are found to be strongly enhanced when the electric field of the linearly polarized laser line is parallel to the *b* axis. For the $CaFeO_{2.5}$ ordered system, strong polarizability of these modes corresponds to strong Raman intensities. Conversely, the apical oxygen disorder observed in low-temperature oxygen-conducting $SrFeO_{2.5}$ destroys the long-range coherence of the respective Raman modes, which consequently show a strongly reduced intensity. This study provides a vibrational tool to discriminate between ordered and disordered isomorporphous $ABO_{2.5}$ Brownmillerite frameworks. Furthermore, in combination with DFT calculations, we have found that the weakening of the interlayer interactions is responsible for the loss of ordering in Brownmillerite compounds.

Keywords: Raman, resonant Raman, Brownmillerite, DFT, disorder systems, $CaFeO_{2.5}$, $SrFeO_{2.5}$

(Some figures may appear in colour only in the online journal)

1. Introduction

The search for oxygen ion conductors that operate at moderate temperatures has attracted considerable interest due to their potential technological application in solid oxide fuel cells (SOFCs) [1–14]. Materials that are presently in use function only at high (900–1000 °C) or intermediate (500–750 °C) [10] temperatures, with consequent chemical and mechanical stability problems over time [9]. Promising materials functioning at moderate temperatures are oxides with Brownmillerite-type structure, oxygen-deficient perovskites with an overall stoichiometry of $ABO_{2.5}$, that show, in some cases, oxygen mobility at ambient temperatures [15–17].

The Brownmillerite framework is an oxygen vacancy-ordered framework consisting of alternating octahedral BO_6 and tetrahedral BO_4 layers. Each $(BO_4)_\infty$ tetrahedra chain bridge can principally point in two directions referred to as L and R, and the space group symmetry of the Brownmillerite framework depends on the symmetry relation between the L and R chains [15, 18–22]. Within the orthorhombic unit cell, a random distribution of all L and R chains results in a special disorder scenario of the $(BO_4)_\infty$ chains that

can be described in the *Imma* space group, implying a split position of the tetrahedral B cations and associated tetrahedral in-plane oxygen atoms. Brownmillerite frameworks showing an ordered $(BO_4)_\infty$ chain arrangement are generally described in the *I2mb* space group, with all tetrahedra pointing in the same direction (only L or R chains are present), or in the *Pnma* space group, with an ordered alternation of L and R chains along the *b* axis.

Symmetry operations of the transformation of the L chain into the R chain and vice versa are also symmetry operations of the underlying perovskite structure, which should lead, in principle, to the same energy configuration for the two sets [19–26]. The L↔R transformation does not change the first coordination spheres of the A and B cations and does not noticeably alter the interatomic distances [17]. Nevertheless, for different combinations of A and B cations, different tetrahedra ordering schemes have been found experimentally [15, 17, 19, 27].

In their studies, Kruger *et al* [24, 25] showed that the thermal expansion of the $CaFeO_{2.5}$ structure causes the distances between the tetrahedral layers to increase disproportionally more compared with the rest of the structure. Due to an increase in the distance between the tetrahedral layers, they hypothesized that it becomes energetically possible to compensate the electron dipoles within each layer. The aperiodic order of the sequence of tetrahedral chains is assumed to minimize the structural distortions otherwise present in a strictly alternating sequence. Moreover, they argued that anti-phase boundaries (APBs) can form if different domains of the *Pnma* structure grow together and make contact, producing thin slabs of *I2mb* structures within the *Pnma* matrix.

In addition, Auckett *et al* [28] have studied the behavior of long-range chain ordering in $Sr_2Fe_2O_5$. They found that the apical oxygen atoms are more mobile than those at other positions and display anisotropic motions in the directions of the tetrahedral layers. Their electron diffraction (ED) patterns suggest that such ordered sequences are present at least locally, and the diffuse intensity lines on these ED patterns arise from areas where the long-range order between the layers is absent.

These findings have been confirmed by the transmission electron microscopy (TEM) work by D'Hondt *et al* [20], in which the diffuse intensity lines on the ED patterns demonstrate that disorder is also present in the stacking sequence of the tetrahedral layers. The TEM investigation clearly revealed that the L and R tetrahedral chains in the $Sr_2Fe_2O_5$ structure form perfect two-dimensional order within the tetrahedral layers according to an -L-R-L-R sequence. Such an arrangement of the tetrahedral chains within the layer is more energetically favorable for the mutual interaction of oppositely oriented electric dipoles associated with the L and R chains because it provides the shortest separation between the different types of chains. However, no significant energy gain is attained in the ordering of the tetrahedral layers because the change of the stacking sequence by a mutual displacement of the layers does not alter the nearest-neighbor separations between the L and R chains. These effects cause the simultaneous presence of areas with differently ordered stacking sequences of the layers and local areas with disordered stacking.

Abakumov *et al* [18] have proposed a model in which a significant part of the tetrahedral chains change their rotation sense so that an L-chain becomes an R-chain, and vice versa, to explain the findings obtained on a Sr_2MnGaO_5 Brownmillerite. The transformation of chains of different types into each other may occur at point defects such as oxygen vacancies or in the presence of a cation with a different coordination, such as a square planar coordination. They suggested as possible driving factors the size of the A and B cations and the electronic configuration of the B cation.

Despite numerous structural data available regarding Brownmillerite compounds and the numerous assumptions regarding the origin of the different structural arrangements, there is not yet clear evidence of what is the driving force causing tetrahedral chain ordering, when present. Little can be determined without using a spectroscopic technique.

To clarify whether the origin of the ordering or disordering of the Brownmillerite structures is connected to the presence or not of specific modifications of intralayer or interlayer interactions, a technique that permits one to gather information on the electron configuration and on the vibrational behavior of the materials is necessary. Raman spectroscopy is one of the most promising because it can look at both properties at the same time. Analysis of the homologous $CaFeO_{2.5}$ and $SrFeO_{2.5}$ systems, the former crystallizing in the ordered *Pnma* structure and the latter showing a disordered arrangement of the tetrahedra that can be indexed in the average *Imma* space group, should allow one to better understand the ordering driving forces.

Here, we present an orientation-dependent Raman analysis of oriented $CaFeO_{2.5}$ single crystals together with first-order and resonant Raman spectra of isostructural Brownmillerite powders. The single-crystal analysis highlighted the anisotropy of the optical response of this system and parallel density functional theory (DFT) calculations on $CaFeO_{2.5}$ helped us to understand the role of electronic interactions in the structural order. A comparison between the Raman spectra collected on (ordered) $CaFeO_{2.5}$ and (disordered) $SrFeO_{2.5}$ powders allowed us to determine the changes in the lattice dynamics involving the apical oxygen atoms that could be used to discriminate between ordered or disordered behavior. DFT methods are, in this context, one of the most promising tools for computational studies of the vibrational and electronic behaviors of complex materials as mixed valence oxides [16, 29–34].

2. Experimental and methods

2.1. Samples

Polycrystalline $CaFeO_{2.5}$ was prepared by intimate mixing, in the presence of acetone, of high-purity $CaCO_3$ (99.95%, Aldrich) and Fe_2O_3 (99.99%, Aldrich) in stoichiometric proportions. Once dried, the mixture was calcined in air at 1273 K for 24 h three times to reach the desired stoichiometry, resulting in a dark red color. The single-crystal $CaFeO_{2.5}$ was synthesized from a polycrystalline sample of $CaFeO_{2.5}$ using an NEC (SC2) image furnace equipped with two 500 W

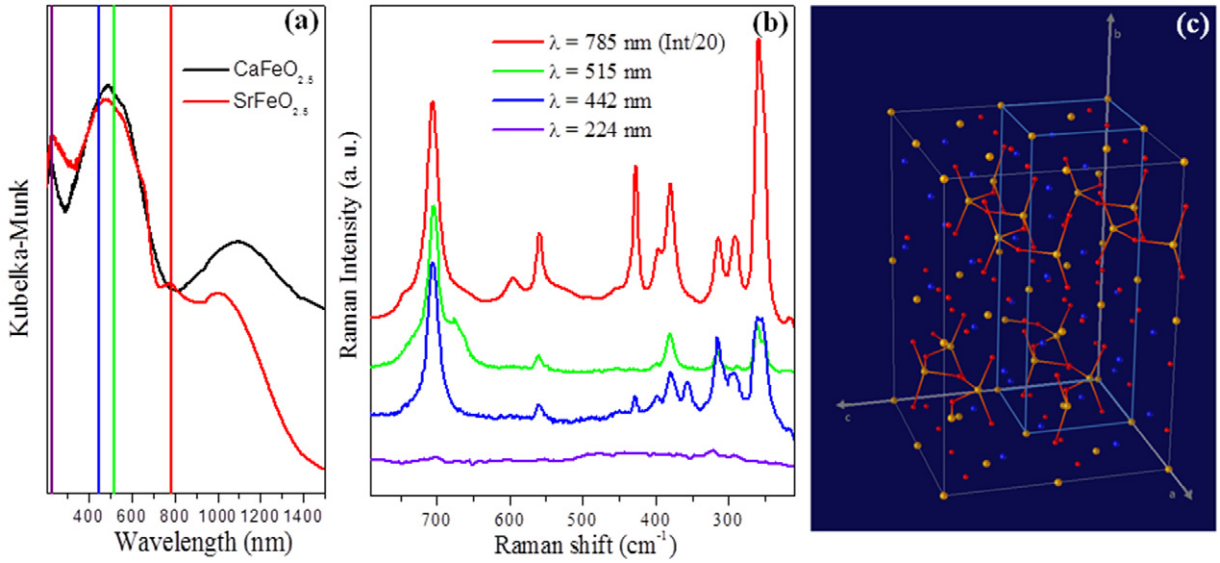

Figure 1. (a) UV-vis DR spectra of $CaFeO_{2.5}$ (black curve) and $CaFeO_{2.5}$ (red curve), with the different laser lines tested in Raman experiments superimposed; (b) Raman spectra collected on system using different laser excitation lines; (c) the crystallographic cell (cyan box) and the $2a \times 1b \times 2c$ supercell (gray box) used for calculations of $CaFeO_{2.5}$. Red balls are oxygen, yellow balls are iron, and blue balls are calcium. For clarity, bonding of the tetrahedra have been included.

halogen lamps and two optical mirrors. A detailed explanation of the method is presented elsewhere [27]. The crystalline quality and precise orientation of the $CaFeO_{2.5}$ single crystal have been previously determined by neutron diffraction on the 5C2 single-crystal diffractometer at the ORPHEE reactor (LLB Saclay, F) [27].

Polycrystalline $SrFeO_{2.5}$ was obtained from a mixture of stoichiometric amounts of $SrCO_3$ (99.9%, Aldrich) and Fe_2O_3 (99.99%, Aldrich). The mixture was calcined in air at 1273 K for 24 h and then ground and pressed into 1 g weight and 13 mm diameter pellets. It is well-known that the oxygen stoichiometry in the $SrFeO_{2.5+x}$ compound is strongly dependent on the temperature and oxygen partial pressure. Therefore, great effort was needed to precisely control the oxygen content and crystalline quality of the $SrFeO_{2.5}$ samples. The best preparation method consisted of a heating step at 1273 K in air for 24 h, followed by an additional annealing step in air at 1473 K for another 24 h. Finally, to reach the exact stoichiometry, the pellets were again annealed at 1273 K for 12 h and then slowly cooled to ambient temperature under vacuum. This method allowed an important reduction of the presence of stacking faults in the structure along the *b* axis.

2.2. UV-Vis spectroscopy

Diffuse reflectance (DR) UV-VIS spectra have been collected with a Varian Cary 5000 spectrometer in the 175–1500 nm range by using the Teflon-coated DR integrating sphere accessory. DR UV-vis spectra of polycrystalline $CaFeO_{2.5}$ and $SrFeO_{2.5}$ diluted 1/20 in weight with Teflon are reported in figure 1(a) as superimposed with the available laser lines on our Raman spectrometers. Both spectra show a similar shape with a weak band centered at 1100 nm, an intense band centered at 500 nm, and an edge in the UV region below 350 nm. Band gap values have been extrapolated from the edge of the adsorption bands, giving 1.28 eV and 1.49 eV for $CaFeO_{2.5}$ and $SrFeO_{2.5}$, respectively.

2.3. Raman spectroscopy

Raman measurements on the oriented single crystal of $CaFeO_{2.5}$ and polycrystalline powders have been performed using an InVia Renishaw Raman Microscope in backscattering geometry, equipped with a 785 nm linearly polarized laser line. Linear polarization is along the *y*-direction, and the optical path is along the *z* direction in our reference system. Polarization analyzer was not present in our configuration. Nevertheless, in our InVia spectrometer, the scattered light is naturally polarized at 80% along the *y*-direction when it scatters on the grating. This $z(y80\%y)$-z configuration allows one to see all vibrational modes with some Raman intensity, but it enhances the A_g modes with respect to the B_g modes. The availability of an oriented single crystal, mounted on a homemade rotating stage with a precision of $\pm 0.5^\circ$, allows one to analyze the orientation-dependent interaction of the electric field ($\boldsymbol{E}$) of the linearly polarized laser with the electronic configuration of the sample (see equations (2) and (3)).

We preformed several measurements with the different excitation lasers present in our laboratory (wavelengths 785, 514, 442, 244 nm) [35–37]. Figure 1(b) shows the Raman spectra collected with the different excitation lasers on the $CaFeO_{2.5}$ system. The 785 nm laser produces a well-defined Raman spectrum, whereas the effects of resonance are evident on spectra collected with 514 and 442 nm lasers, where intensities are enhanced only for specific bands. Finally, the far-UV line at 224 nm resulted in an almost featureless flat Raman spectrum. For this reason, we choose the 785 nm laser wavelength for first-order Raman measurements, which avoided resonance effects due to direct transitions to real electronic states (figures 1(a) and (b)), to compare with

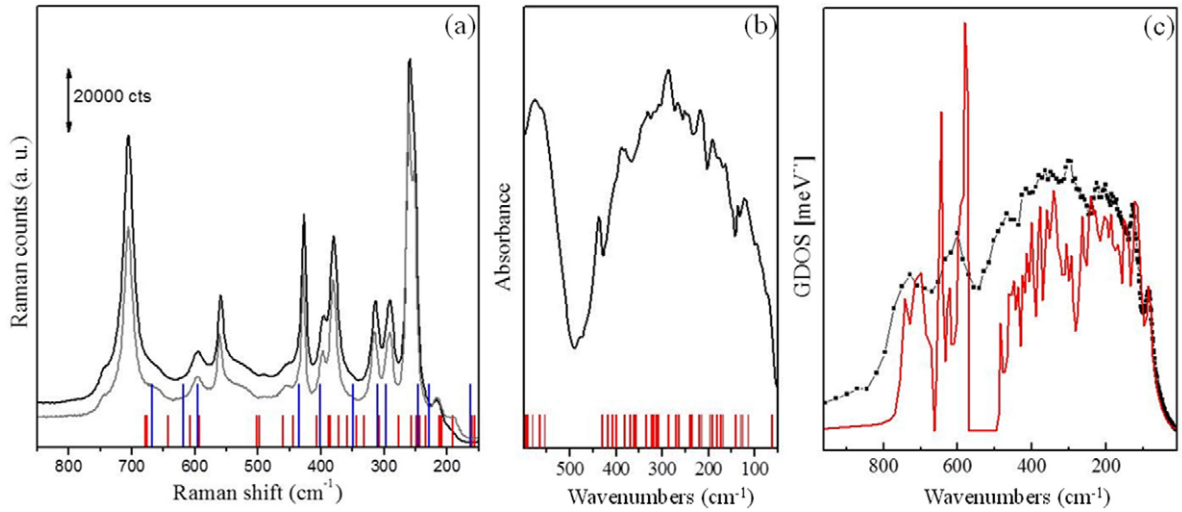

Figure 2. (a) Raman spectra in the $z(y\ 80\%\ y)$-z scattering configuration of powdered $CaFeO_{2.5}$ from ground single crystal (black curve) and $CaFeO_{2.5}$ from polycrystalline synthesis (gray curve) superimposed with the frequencies of the calculated Raman-active modes: blue bars represent A_g mode; red bar, B_g modes. (b) ATR-IR spectrum of polycrystalline $CaFeO_{2.5}$ superimposed with the frequencies of the calculated IR active modes. (c) Experimental vibrational DOS from the INS experiment (from [16], black scattered points) superimposed with the calculated GDOS (this work, red line). Parts (a) and (b) unpublished results; part (c) adapted with permission from [16], copyright (2008) American Chemical Society.

Raman frequencies from DFT calculation. Instead, we made use of both first-order and resonant Raman techniques to analyze in detail the differences between ordered $CaFeO_{2.5}$ and disordered $SrFeO_{2.5}$.

The maximum power used was 1% of the total laser power of approximately 100 mW to avoid radiation damage problems. The spectra reported here were obtained by averaging five subsequent spectra, with each of them collected with an integration time of 20 s cm^{-1}. Acquisition parameters were all kept fixed during the experiments to allow direct comparison among the spectra collected with different sample configurations.

2.4. Inelastic neutron scattering

The inelastic neutron scattering (INS) measurements were performed on the cold neutron time-of-flight spectrometer IN6 at the ILL [16]. The incident wavelength was 4.12 Å and neutrons were detected over the scattering angles from 13° to 114° 2Θ.

We used a slightly inelastic focusing ($E_{focus} = 2.7$ meV) to improve resolution at large energy transfers in up-scattering (neutron energy gain mode). The raw data were corrected for empty container scattering and normalized to a vanadium standard. The spectra thus obtained were converted into generalized phonon density of states (GDOS) $G(\omega)$ using the incoherent approximation. Multiphonon corrections were performed self-consistently [38].

2.5. Infrared spectroscopy

Attenuated total reflectance (ATR) FT-IR spectra were collected at 4 cm^{-1} resolution in the far-IR region (10–600 cm^{-1}) on a Vertex70 Bruker instrument equipped with the PLATINUM ATR adopting a single reflection diamond crystal. The polycrystalline sample of $CaFeO_{2.5}$ was accurately ground in a mortar down to a fine powder to guarantee good contact between the sample and the diamond crystal.

2.6. Computational details

DFT calculations have been performed on the $CaFeO_{2.5}$ system using the VASP code [39]. Calculations were performed at the level of the Kohn–Sham DFT (KS-DFT) using a plane waves basis set, a PAW-type pseudopotential, and a Perdew, Burke and Ernzerhof (PBE) exchange-correlation functional with a total number of 43 419 plane-waves (cutoff 800 eV). Six, 8, and 8 valence electrons are used for O, Ca, and Fe, respectively. For both the one electron and vibrational properties, the crystallographic cell was extended in a $2a \times 1b \times 2c$ supercell, size $10.8 \times 14.7 \times 11.2$ $Å^3$, to determine long-range Coulomb interactions (figure 1(c)). For computing the vibrational modes, a Monkhorst Pack scheme has been used including only the Gamma point. The force constant matrix has been obtained by the direct method with ionic displacements of 0.03 Å and used as input in PHONON 5.1 software [40, 41] to compute the dynamical matrix and extract eigenfrequencies, phonon polarizations, Raman activities, and IR activities. Raman and IR intensities could not be calculated with these codes, but we were able to compute the GDOS for neutron scattering. Computed frequencies are systematically underestimated at the PBE level of theory due to the lack of exact exchange. To compare with experiments, a scaling factor of 1.07 was obtained by a fitting procedure in accordance with previous works [42, 43].

3. Results and discussion

According to our previous single crystal neutron diffraction study [27], the structure of $CaFeO_{2.5}$ is orthorhombic with

Pnma space group with associated lattice parameters $a = 5.430(2)$ Å, $b = 14.76(2)$ Å and $c = 5.601(4)$ Å. It belongs to the general point group D_{2h} (mmm) [44]. From a structural point of view, $CaFeO_{2.5}$ shows three atoms residing in the 8d Wyckoff position, two in the 4c position, and only one in the 4a position [27]. Decomposition of the reducible representation of the group of vibrational modes in the $CaFeO_{2.5}$ crystal in terms of its irreducible representations is as follows [45, 46]:

$$\Gamma = 13A_g+14A_u+11B_{1g}+16B_{1u}+13B_{2g}+14B_{2u}+11B_{3g}+16B_{3u}. \quad (1)$$

The structure of $CaFeO_{2.5}$ comprises 105 vibrational modes, after removal of the three translations, which can be classified as follows: (i) 48 only Raman-active; (ii) 43 only IR-active; (iii) 14 IR- and Raman-silent. The Fe atom in the 4a Wyckoff position, i.e., in octahedral coordination, does not move for any Raman-active mode.

The Raman activity is connected with the electric field **E** of the excitation light and the Raman tensor $\mathscr{R}$ by the following relation [47]:

$$p = \mathscr{R}E, \quad (2)$$

where $\mathscr{R}$ can be decomposed with respect to the point symmetry as follows:

$$\mathscr{R}_{Ag} = \begin{pmatrix} a & 0 & 0 \\ 0 & b & 0 \\ 0 & 0 & c \end{pmatrix}; \quad \mathscr{R}_{B1g} = \begin{pmatrix} 0 & d & 0 \\ d & 0 & 0 \\ 0 & 0 & 0 \end{pmatrix}$$
$$\mathscr{R}_{B2g} = \begin{pmatrix} 0 & 0 & e \\ 0 & 0 & 0 \\ e & 0 & 0 \end{pmatrix}; \quad \mathscr{R}_{B3g} = \begin{pmatrix} 0 & 0 & 0 \\ 0 & 0 & f \\ 0 & f & 0 \end{pmatrix}. \quad (3)$$

It is then clear than in a Raman experiment with $z(y\ 80\%y)\text{-}z$ scattering geometry, it is possible to selectively favor the $\mathscr{R}_{Ag}$ component and, in it, the a, b, or c component by opportunely rotating a single crystal with respect to the spectrometer axes. Whether a Raman-active phonon can be observed under certain experimental conditions regarding the incoming and scattered polarization is determined by

$$I_s \propto |e_i \cdot \mathscr{R} \cdot e_s|^2 . \quad (4)$$

Figure 2(a) shows the Raman spectra collected for the $CaFeO_{2.5}$ sample ground either from the single crystal (black curve), so potentially textured, or from an independent polycrystalline synthesis (gray curve). In the powder grained from single crystal, the texturing effect is not present (or not appreciable) and the two spectra are similar except for a different amount of background fluorescence. Due to the adopted scattering geometry, in such spectra the A_g modes should be preferentially selected and we can therefore assign the most intense bands at frequencies at 705, 455, 381, 316, 290, 263, 253, and 188 cm^{-1} to the A_g symmetry. For the same reason, few less intense bands can be seen in spectra of figure 2 and can be assigned to B_g modes.

To perform a complete vibrational mode analysis of the $CaFeO_{2.5}$ sample, we performed complementary infrared and INS experiments. The ATR FT-IR spectrum is shown in figure 2(b). Several modes can be barely resolved above a broad dominating peak in the region 50–450 cm^{-1}, whereas a unique unresolved broad peak includes all frequencies of approximately 600 cm^{-1}.

Table 1. Table summarizing the experimental and calculated frequencies of the Ag Raman active modes as shown in figure 2(a).

A_g exp. freq. (cm^{-1})	A_g calc. freq (cm^{-1})	|Relative error|
251	226	0.09
261	246	0.06
292	297	0.02
313	310	0.01
380	350	0.08
393	400	0.02
428	435	0.02
558	596	0.09
595	618	0.04
705	668	0.05

The GDOS from the inelastic neutron experiment on $CaFeO_{2.5}$ is shown in figure 2(c). Vibrational modes below 150 cm^{-1} are well-resolved, whereas at a higher frequency the large quantity of modes with similar mode frequencies and the reduced resolution concur in producing large and smoothly varying peaks.

From the experimental results shown in figure 2, it is clear that Raman measurement with linearly polarized light and oriented single crystals is the most suitable way to perform an unambiguous mode assignment and to look at spectral features that can be connected with the structure ordering. Nonetheless, it is important to use all three complementary spectroscopic techniques all together to perform an exhaustive comparison with simulations. We performed periodic KS-DFT simulations of the $CaFeO_{2.5}$ structure to obtain the eigenfrequencies and polarizations for all Raman-active, IR-active, and INS vibrational modes.

Calculated Raman-active modes are shown as bars in figure 2(a), with the blue one representing A_g modes and red ones representing all the other B_g modes. The comparison between the experimental frequencies for the A_g modes and the calculated frequencies in the range 200–800 cm^{-1} is presented in table 1, revealing a quite satisfactory match with the majority of modes in accordance with a relative error less than 4%. The three A_g modes lying below 200 cm^{-1} cannot be experimentally detected due to the notch filter intensity suppression. The calculated vibrational polarizations for the assigned A_g modes are shown in figure 3. It is worth noticing that the majority of these modes show enhanced displacement along the b-axis direction, particularly for the apical oxygen ions.

Calculated IR-active modes are shown as red bars in figure 2(b). The qualitative agreement is satisfactory, including the perfect reproduction of the vibrational gap at approximately 500 cm^{-1}. Nevertheless, due to the large number of IR-active vibrational modes (43) for this complex structure, an exact mode assignment is not possible without ambiguity.

The calculated GDOS is the red curve in figure 2(c). In this case, there is good agreement in both band frequencies and relative intensities all along the spectrum with respect to experimental data. Bands are well-resolved below 150 cm^{-1}, where our Raman spectra are blind. In this region, vibrations

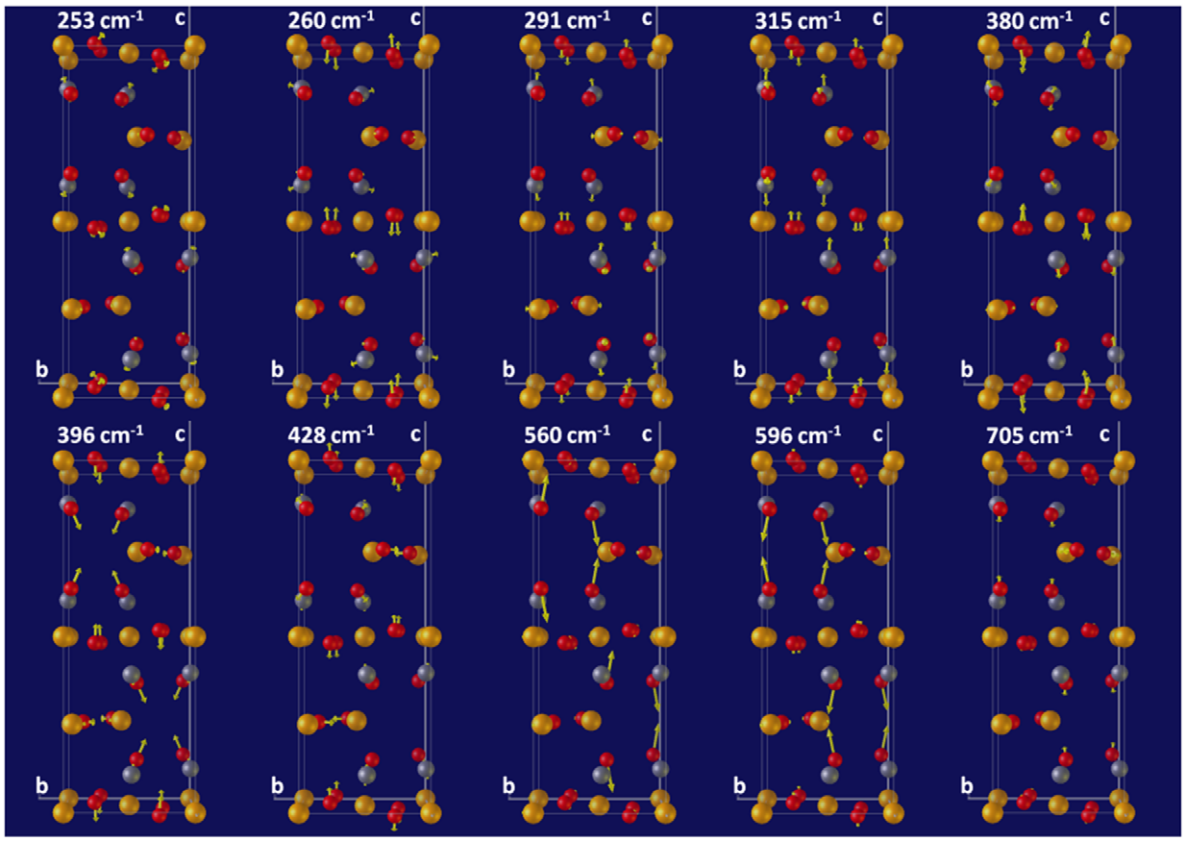

Figure 3. Computed polarizations for the A_g modes that have been assigned in Raman scans for the $CaFeO_{2.5}$ system (table 1). Many of these modes show a marked phonon polarization of apical oxygen displacements along the *b* direction. Atomic species are Ca (blue), Fe (yellow), and O (red).

are dominated by the movements of the Ca cation. On the contrary, the breathing and stretching modes in the region at approximately 700 cm^{-1} are all convoluted in a broad peak in the GDOS, whereas we can easily resolve different modes in the Raman spectra.

From DFT results, it is also possible to gain a more detailed insight into the peculiar electronic arrangement that may explain the preference of $CaFeO_{2.5}$ for the *Pnma* space group compared to *I2mb* or disordered *Imma*. Both structure models in *Pnma* and *I2mb* have been relaxed at a rather high level of precision and both simulations converged, showing a comparable ground state energy that is *Pnma* energetically and is slightly favored by only 0.09 eV (8.68 kJ mol^{-1}). The results of the geometry optimizations are reported in table 2. Both simulations converged to similar lattice parameters and differ by less than 2% from the experimental parameters. There is no residual stress in both structures and residual forces are less than 10^{-4} eV A^{-1}, except along the *a* direction in *I2mb* structure. The origin is a residual non-compensated force from ions and dipoles along the *a* axis (chain direction). This finding supports the idea that the origin of the type of ordering in Brownmillerite structures is the competition between interacting dipole moments and charge distributions.

The analysis of the electronic DOS for the $CaFeO_{2.5}$ system in the *Pnma* structure pointed out a computed band gap of 1.36 eV. Our calculated value corresponds well to the one extracted from UV-Vis measurements (1.28 eV) with a misfit of approximately 5%. This small error does not significantly affect our vibrational analysis.

Analyzing the electron density output for the *Pnma* case, shown in figure 4(a), it is clearly evident that the apical oxygen is more strongly bonded to the tetrahedral rather than the octahedral Fe atoms. This implies the presence of induced local dipoles along the *b*-axis direction. Unbalanced charge distribution is not observed in the *ac* planes cut at the octahedral plane (figure 4(b)). In the tetrahedral (figure 4(c)) layers, even if a symmetrical charge density is observed for all Fe–O bonds along each chain, the empty space between them gives unbalanced charge distributions and induced by dipole moments along *c*-axis direction.

The strength of the induced electronic dipole interactions depends on the overlap of crystalline orbitals along the dipole moment direction. The possibility that induced electric dipoles, produced by the anisotropic distribution of charges along *b* direction, could interact coherently on a long-range scale depends mainly on the amount of orbital overlap of $Fe_{octa} - O_{ap}$ bonds (figure 4(a)). When this interaction exists it can be easily distorted by an external electric field, implying high polarizability along that direction. In this way, a perturbation along the *b* axis by the electric field of a laser is expected to produce intense Raman modes [48]. On the contrary, due to the scarce orbital overlap between two chains along the *c*-direction, the polarizability should be weaker.

To extend our analysis of electron density maps, we performed a bond order analysis as implemented in the VESTA

Table 2. Results from the geometry optimization of $CaFeO_{2.5}$ in the *Pnma* and *I2mb* space groups. For comparison, experimental lattice parameters are also reported. An interesting finding is that in *I2mb* calculation, there is a residual non-compensated force from ions and dipoles along the *a* axis (chains direction).

	Pnma	*Ic2m*[a]	Exp, from [27]
a (Å)	5.31	5.29	5.430(2)
b (Å)	14.58	14.58	14.76(2)
c (Å)	5.46	5.47	5.601(4)
Energy (eV)	−996.29	−996.20	
Total force (eV $Å^{-1}$) (*a*; *b*; *c*)	1.0E−4; 0.0; 3.9E−4	6.0E−3; 3.2E−5; 3.5E−4	
Ion+dipol force (eV $Å^{-1}$) (*a*; *b*; *c*)	0.26; 0; 0.2	−29.8; −0.09; −0.01	
Stress (kB)	0	0	

[a] *Ic2m* is the same space group of *I2mb* with permutated axes in the order they corresponds to that of *Pnma*.

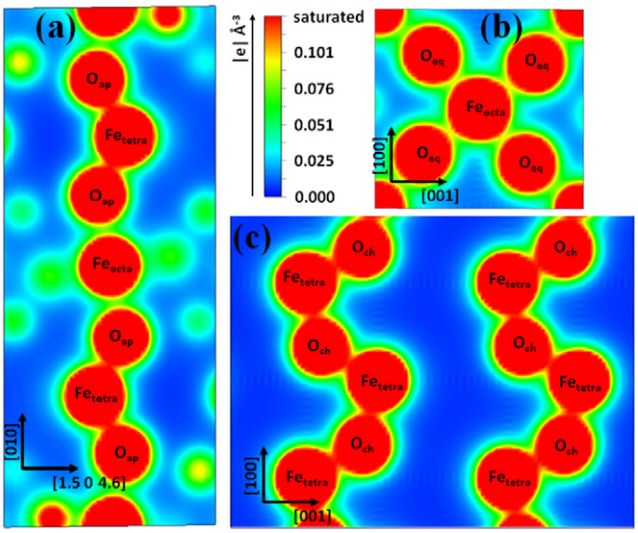

Figure 4. Electron density maps for the $CaFeO_{2.5}$ system in the *Pnma* space group: periodic DFT simulations with VASP code [39]. Octahedral and tetrahedral Fe atoms are labeled as Fe_{octa} and Fe_{tetra}, respectively, whereas O_{ap}, O_{eq}, and O_{ch}, refer to the oxygen atoms bridging $Fe_{octa} - Fe_{tetra}$, $Fe_{octa} - Fe_{octa}$, and $Fe_{tetra} - Fe_{tetra}$, respectively. (a) Plane including O_{ap}, Fe_{octa}, and Fe_{tetra} atoms, with the *b* axis vertical. (b) The *ac* plane intercepting Fe_{octa}. (c) The *ac* plane intercepting Fe_{tetra}. To allow better resolution in the lower electron density region between adjacent atoms, the color scale has been chosen in a way that it saturates in the proximity of the nuclei; in this way, Fe and O atoms have apparently the same electron density.

software [49] on the FeO_6 (O_h) FeO_4 (T_d) polyhedra. As input, we considered a Fe^{3+} formal valence and a bond valence parameter $\rho = 1.765$ [50]. Salient results are presented in table 3. The calculated bond length corresponds well to the average value and the calculated coordination numbers (CNs) correspond well to the expected values for both FeO_6 and FeO_4.

Interestingly, a large distortion index is calculated for the FeO_6 unit compared to the almost undistorted FeO_4. This has clear consequences for the fraction of charge Δq that O ions receive from Fe_{octa} or Fe_{tetra}. The Fe_{tetra} shares a large and identical fraction of charge with all surrounding O ions. On the contrary, Fe_{octa} shares less charge with surrounding O ions than Fe_{tetra} (on average approximately 20% less) and, in the octahedron itself, shares 7% less with O_{ap} than with $O_{octa,eq}$.

Results from bond order analysis corroborate our interpretation in which there is an unbalanced charge

Table 3. Results from bond order analysis performed on the octahedron unit FeO_6 (O_h) and tetrahedron unit FeO_4 (T_d). Formal valence for Fe has been set to 3+. Δq refers to the fraction of charge received by oxygen atoms from the central Fe cation.

	FeO_6 (O_h)	FeO_4 (T_d)
Average bond length	2.00 Å	1.84 Å
Distortion index	0.018	0.003
Effective CN	5.9	4.0
$\Delta q O_{eq}$	0.54	0.74
$\Delta q O_{ap}$	0.42	0.76
Bond valence sum	3.2	3.3
Expected bond length	2.02 Å	1.87 Å

between octahedral and tetrahedral units that produce induced electronic dipoles in the different layers. Furthermore, it highlights that the elongation of the *b* axis weakens the $Fe_{octa} - O_{ap}$ bond to a limit when electronic overlap is so weak that no more correlation exists between induced electric dipoles in different layers.

To verify our interpretation with some spectroscopic evidence, we performed a series of non-resonant and resonant Raman experiments using powders and single crystals. The results of the orientation-dependent Raman experiments using the $CaFeO_{2.5}$ single crystal are presented in figure 5. Measurement with the $\boldsymbol{E}$ vector in the (*a*, *b*), (*b*, *c*), and (*a*, *c*) planes are shown in figures 4(a), (b), and (c), respectively. The most striking and interesting findings were obtained when the sample was rotated in such a way that $\boldsymbol{E}$ moves from parallel to perpendicular to the *b* axis (figures 4(a) and (b)). In such experiments, the A_g modes at 705, 455, 381, 316, 290, 263, 253, and 188 cm^{-1} are significantly enhanced when $\boldsymbol{E}//b$, and the enhancement progressively disappears when $\boldsymbol{E}$ moves toward the *a*- or *c*-axis. Final support of this picture is reported in figure 5(c), where the *b*-axis is out of the scattering plane and no significant differences are observed along the crystal rotation.

To correlate this striking orientation dependence of the Raman spectra of the $CaFeO_{2.5}$ system with the oxygen ordering properties of isomorphous Brownmillerite systems, we compared Raman spectra of $SrFeO_{2.5}$ and $CaFeO_{2.5}$ powders (figure 6 red versus black or gray curves). In the Raman spectra collected on $CaFeO_{2.5}$ powders, the A_g modes at 705, 455, 381, 316, 290, 263, 2.53, and 188 cm^{-1} are still very strong; a fraction of crystallites have the *b*-axis partially

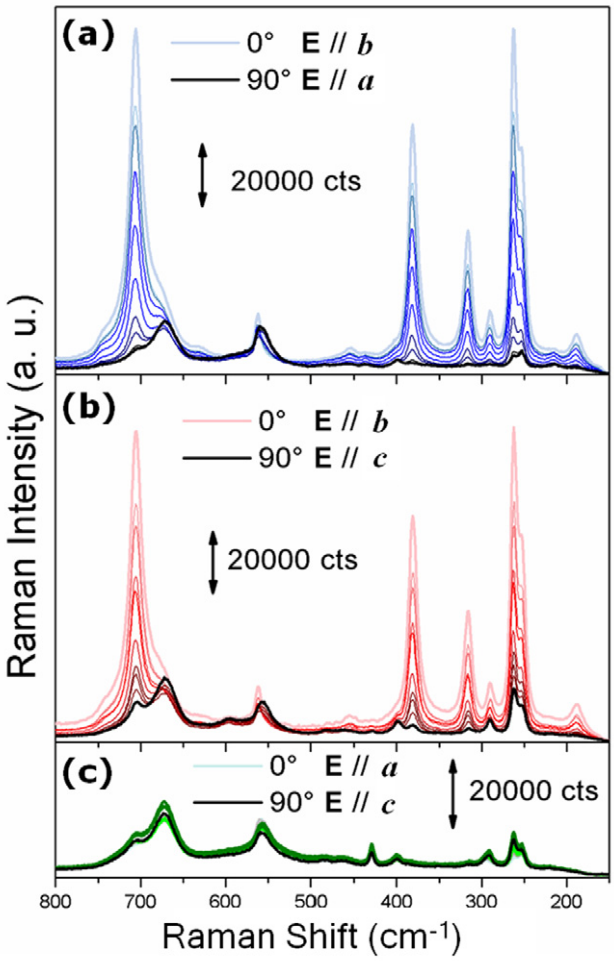

Figure 5. Raman spectra of $CaFeO_{2.5}$ single crystal for different orientations. From pale to black color, nine spectra have been collected every 10° of rotation in the scattering plane: (a) *a* and *b* axis in the scattering plane; (b) *b* and *c* axis in the scattering plane; and (c) *a* and *c* axis in the scattering plane. The laser excitation light was $\lambda = 785$ nm. The spectra are collected in $z(y\ 80\%y)$-z geometry and rotating the single crystal into the scattering plane.

oriented along *E*. The same random orientation of the *b*-axis holds for the $SrFeO_{2.5}$ powders, too; however, that does not show any strong Raman feature. Actually, the Raman spectrum of $SrFeO_{2.5}$ powders looks like the spectra of the $CaFeO_{2.5}$ system collected with $\boldsymbol{E}$ in the *ac* plane (figure 5(c)). The structural changes obtained replacing Ca by Sr are mainly observed along the *b*-axis, where the $Fe_{octa}-O_{ap}$ distances vary significantly from 2.12 to 2.20 Å, whereas both $Fe_{octa}-O_{eq}$ and $Fe_{tetra}-O_{ap}$ distances are much less affected by the A-cation nature [17, 28]. Moreover, as reported by other authors [20], $SrFeO_{2.5}$ shows disorder along the *b* stacking direction.

The interlayer distance (along *b*-axis) of the interacting induced electronic dipoles can be taken as the mid distance between the nearest $Fe_{tetra}-O_{ap}$ in two successive layers, i.e., 5.7 Å for $CaFeO_{2.5}$ and 6.1 Å for $SrfeO_{2.5}$. The distance between the two chains that should correspond to the interaction range of intralayer-induced (along *c*-axis) electronic dipoles is 5.6 Å for $CaFeO_{2.5}$ and 5.7 Å for $SrFeO_{2.5}$. The intralayer and interlayer interactions both participate in the ordering process because there is no advantage in compensating induced electric dipole interlayer or intralayer.

We showed that for $CaFeO_{2.5}$ the interlayer interactions are present (figure 5) and, from the similarity of the distance with intralayer interactions, we can affirm that the two are in competition and create a three-dimensional ordered structure. On the contrary, we showed that for $SrFeO_{2.5}$ the interlayer interactions are suppressed, or greatly reduced (figure 6(a)), and this is in accordance with the disproportionate increase of the interlayer interaction distance with respect to the intralayer distance. The decreased orbital overlap of $Fe_{octa}-O_{ap}$ has, as a consequence, a decrease in the interaction strength and correlation length of interlayer interacting electronic dipoles. This, in turn, makes compensating the interacting electronic dipoles only on intralayers more advantageous.

The Raman spectra reported in figure 6(b) have been collected under resonant Raman conditions (figure 2(a)), and the 442 nm line particularly excites orbitals participating in the total-symmetric stretching mode at 700 cm^{-1}. In the spectrum of $CaFeO_{2.5}$, this mode is by far the most intensely appreciable under resonant conditions using a 442 nm excitation source. This means that its relative intensity with respect to the other adjacent modes has been increased by one order of magnitude due to the resonant condition. For the framework total-symmetric stretching, the mode should be similar to $CaFeO_{2.5}$, and then the resonance condition would similarly apply (figure 1(a)). In the $SrFeO_{2.5}$ spectrum of figure 6(b), the mode at 662 cm^{-1} is the one that is the most enhanced, and we assigned it to the total-symmetric breathing mode of tetrahedra and octahedra units of $SrFeO_{2.5}$. These results highlight that in both samples, the alternating octahedral plus tetrahedral blocks (as specific units of the structure) are present and that the consistent shift in frequency of the vibration suggest a different bond force constant.

In the non-resonant case (figure 6(a)), the breathing mode of octahedra is almost one order of magnitude less intense for the $SrFeO_{2.5}$ system than in the $CaFeO_{2.5}$ system, whereas their relative intensity is comparable in the resonant case (figure 6(b)). This can be explained by the fact that resonant Raman excites vibrational modes of the same local unit engaged in the electronic transition and exhibiting the same symmetry [35, 36, 51–53], whereas in the first-order Raman probe the spatial coherence of all the units vibrates together. Moreover, the full width at half maximum (FWHM) obtained by fitting the mode in non-resonant conditions with a Lorentzian line shape is 19.6 cm^{-1} for $CaFeO_{2.5}$, whereas it is 26.8 cm^{-1} for $SrFeO_{2.5}$. This highlights a damping effect in the latter system connected to the shorter coherence length of this lattice vibration.

The same mode appears red, shifted by $\Delta\tilde{\nu} = 43\ cm^{-1}$ in the case of $SrFeO_{2.5}$. For a total-symmetric A_g stretching mode, the frequency ($\omega = c\tilde{\nu}$, where *c* is the speed of light) can be directly related to the equilibrium $Fe_{octa}-O$ bond distance through the force constant (k) and the reduced mass (μ) of the oscillator ($\omega = \sqrt{(k/\mu)}$ in the harmonic approximation. Considering a single $Fe_{octa}-O$ vibration (where μ is the same in both systems), calculation of the force constants gives a value of 366 N m^{-1} for the Ca-containing material and

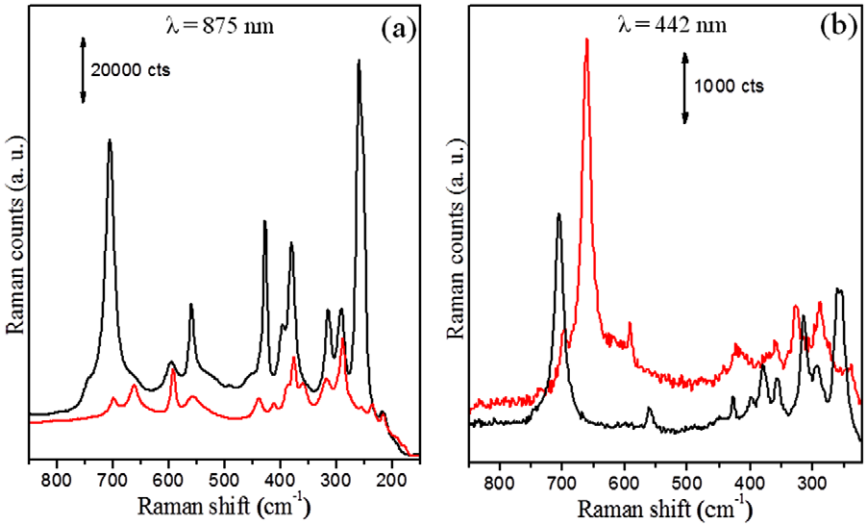

Figure 6. Raman spectra of $CaFeO_{2.5}$ (black line) and $SrFeO_{2.5}$ powder (red line). For the $SrFeO_{2.5}$ system, only polycrystalline samples are available. (a) Scans with laser excitation light at $\lambda = 785$ nm. (b) Scans in resonance mode with laser excitation light at $\lambda = 442$ nm. Note that the total-symmetric breathing mode on $SrFeO_{2.5}$ at 662 cm^{-1} is almost suppressed in non-resonant Raman but is visible when resonantly excited.

322 N m^{-1} for the Sr-containing material. This corresponds to a decrease in the restoring force of approximately 10% for the latter system. Axes *a* and *c* do not vary considerably for the two systems; therefore, in $Fe_{octa} - O_{eq}$ bonds, force is 1.967 Å for $CaFeO_{2.5}$ and force is 1.985 Å for $SrFeO_{2.5}$. This decrease of the restoring force is directly related to the difference in the $Fe_{octa} - O_{ap}$ bond (2.11 Å for $CaFeO_{2.5}$ and 2.20 Å for $SrFeO_{2.5}$). All these findings are in agreement with O_{ap} in $SrFeO_{2.5}$ being weakly bonded to the octahedron unit and more easily able to separate from it. The $SrFeO_{2.5}$ systems can be then better modeled as a succession of tetrahedra and square planar layers where interlayer interactions are weakened or totally hindered by the reduced overlap of orbitals of apical oxygen with the square plane orbitals.

Analogously, the rocking mode at 263 cm^{-1} for the $CaFeO_{2.5}$ system (see figure 6(a)) should be slightly red-shifted for the $SrFeO_{2.5}$ material. A $\Delta\tilde{\nu}$ value smaller than 43 cm^{-1} is expected because the $Fe_{tetra} - O_{ap}$ bond lengths are much more similar in the two systems (1.862 Å for $CaFeO_{2.5}$ and 1.848 Å for $SrFeO_{2.5}$). A band at 235 cm^{-1} is observed in the $SrFeO_{2.5}$ spectrum reported in figure 6(a). The low intensity of such a mode, with respect to the sharp intensity reported for $CaFeO_{2.5}$, points out the more localized nature of the crystal orbitals involved that produce less intense induced dipoles that, in turn, give less intense Raman bands.

4. Conclusions

Our work is focused on the understanding, from a spectroscopic point of view, of the origin of disorder in Brownmillerite structures. It has been supposed many times that competition between interlayer and intralayer interactions plays a role in defining the specific atomic arrangements. By comparing the ordered $CaFeO_{2.5}$, which showed pronounced Raman effects with the disordered $SrFeO_{2.5}$, results with our calculation for the ordered system, we were able to verify this assumption.

Our simulations have shown that there is a net dipole formed between $Fe_{octa} - Fe_{tetra}$ in the different layers coming from a non-balanced charge due to the different covalency and bond distances of $Fe_{tetra} - O_{ap}$ and $Fe_{octa} - O_{ap}$ bonds. In the orientation-dependent measurements here presented, we observed that, in the highly ordered $CaFeO_{2.5}$ system, intense bands emerge when the electric field of the laser is parallel to the *b* axis.

If there is a dipole–dipole interaction between two layers, then we expect a laser line can perturb it due to strong anisotropy of the charge distribution and the relative long range of this interaction. In this case, when the laser line is parallel to the direction of this interaction, i.e., in the *b* direction in our case, we expect large polarizabilites and consequent high Raman intensities. The relatively short *b*-axis (14.77(2) Å) of the $CaFeO_{2.5}$ system [27], with respect to the $SrFeO_{2.5}$ system ($b = 15.738(8)$ Å) [15], makes the interlayer dipole–dipole interaction effective, forcing the structure to belong to the *Pnma* space group. On the contrary, if the dipole–dipole interaction is not present, or weak, we expect that long-range interlayer organization of charges would not be present and consequently, the polarizability from deformation of more localized charges should be highly damped and therefore the intensities should be weaker. We showed, by non-resonant Raman and resonant Raman techniques, that this is the case for the $SrFeO_{2.5}$ system. The longer *b*-axis of the $SrFeO_{2.5}$ system (15.738(8) Å) [15] weakens the interaction between $Fe_{octa} - O_{ap}$ bonds and consequently results in less interacting dipoles, making them energetically almost equivalent to any orientation of the tetrahedra between different layers. No particular disordering fingerprint have been found for the *a* and *c* directions.

In this work we have identified spectroscopic evidence for the origin of disorder by performing resonant and non-resonant

Raman experiments. In this regard, Raman measurements can be used as a laboratory technique to verify ordering properties of Brownmillerite systems and to investigate the origin of different ordering schemes in specific electronic interactions.

There is now agreement that the onset of disordering is linked with specific lattice modes that trigger low-temperature oxygen mobility. The loss of interlayer ordering (i.e., loss of ordering in the *b* direction) is associated, for the mixed valence Brownmillerite materials, with an anomalous displacement of O_{ap} species. The observed formation of extended-phase boundaries in these materials starting from an ordered structure can be accomplished only with a collective motion of these oxygen species. A single hopping mechanism requires an excessively high-energy barrier to be possible at moderate temperatures and will certainly destroy chain ordering within the *ac* plane (this is a fact that has not yet been found). Our scheme is consistent with the two-step collective mechanism of oxygen mobility ($O_{ap} \rightarrow O_{eq'}$ and $O_{eq''} \rightarrow O_{ap}$) presented by Paulus *et al* [16]. If, from one side, it is able to explain the formation of interlayer disorder while intralayer order is maintained, then the same mechanism is the basis of the known oxygen mobility of SFO at moderate temperatures. The combined understanding of the origin of disorder and the forces triggering moderate temperature ionic mobility can help in the design of Brownmillerite structures for efficient solid-state fuel cells.

Acknowledgments

We are grateful to A Damin (University of Turin, I) for the help in the Raman laboratory. CL received support from the Mega-grant of the Russian Federation Government to support scientific research at Southern Federal University (No.14.Y26.31.0001).

The authors declare no competing financial interest.

References

[1] Mamak M, Coombs N and Ozin G 2000 *J. Am. Chem. Soc.* **122** 8932
[2] Dusastre V and Kilner J A 1999 *Solid State Ion.* **126** 163
[3] Goodenough J B 2003 *Annu. Rev. Mater. Res.* **33** 91
[4] Ormerod R M 2003 *Chem. Soc. Rev.* **32** 17
[5] Zhu W Z and Deevi S C 2003 *Mater. Sci. Eng.* A **362** 228
[6] Mamak M, Metraux G S, Petrov S, Coombs N, Ozin G A and Green M A 2003 *J. Am. Chem. Soc.* **125** 5161
[7] Adler S B 2004 *Chem. Rev.* **104** 4791
[8] Zuo C, Zha S, Liu M, Hatano M and Uchiyama M 2006 *Adv. Mater.* **18** 3318
[9] Tsipis E V and Kharton V V 2008 *J. Solid State Electrochem.* **12** 1367
[10] Brett D J L, Atkinson A, Brandon N P and Skinner S J 2008 *Chem. Soc. Rev.* **37** 1568
[11] Jacobson A J 2010 *Chem. Mater.* **22** 660
[12] Cai Z H, Kuru Y, Han J W, Chen Y and Yildiz B 2011 *J. Am. Chem. Soc.* **133** 17696
[13] Shin T H, Ida S and Ishihara T 2011 *J. Am. Chem. Soc.* **133** 19399
[14] Munoz-Garcia A B, Bugaris D E, Pavone M, Hodges J P, Huq A, Chen F L, zur Loye H C and Carter E A 2012 *J. Am. Chem. Soc.* **134** 6826
[15] Le Toquin R, Paulus W, Cousson A, Prestipino C and Lamberti C 2006 *J. Am. Chem. Soc.* **128** 13161
[16] Paulus W, Schober H, Eibl S, Johnson M, Berthier T, Hernandez O, Ceretti M, Plazanet M, Conder K and Lamberti C 2008 *J. Am. Chem. Soc.* **130** 16080
[17] Piovano A, Agostini G, Frenkel A I, Bertier T, Prestipino C, Ceretti M, Paulus W and Lamberti C 2011 *J. Phys. Chem.* C **115** 1311
[18] Abakumov A M, Alekseeva A M, Rozova M G, Antipov E V, Lebedev O I and Van Tendeloo G 2003 *J. Solid-State Chem.* **174** 319
[19] Abakumov A M, Kalyuzhnaya A S, Rozova M G, Antipov E V, Hadermann J and Van Tendeloo G 2005 *Solid State Sci.* **7** 801
[20] D'Hondt H, Abakumov A M, Hadermann J, Kalyuzhnaya A S, Rozova M G, Antipov E V and Van Tendeloo G 2008 *Chem. Mater.* **20** 7188
[21] Krekels T, Milat O, Vantendeloo G, Amelinckx S, Babu T G N, Wright A J and Greaves C 1993 *J. Solid State Chem.* **105** 313
[22] Lambert S, Leligny H, Grebille D, Pelloquin D and Raveau B 2002 *Chem. Mater.* **14** 1818
[23] Hadermann J *et al* 2007 *J. Mater. Chem.* **17** 692
[24] Kruger H and Kahlenberg V 2005 *Acta Crystallogr.* B **61** 656
[25] Kruger H, Kahlenberg V, Petricek V, Phillipp F and Wertl W 2009 *J. Solid State Chem.* **182** 1515
[26] Lazic B, Kruger H, Kahlenberg V, Konzett J and Kaindl R 2008 *Acta Crystallogr.* B **64** 417
[27] Ceretti M, Piovano A, Cousson A, Berthier T, Meven M, Agostini G, Schefer J, Hernandez O, Lamberti C and Paulus W 2012 *CrystEngComm* **14** 5771
[28] Auckett J E, Studer A J, Pellegrini E, Ollivier J, Johnson M R, Schober H, Miiller W and Ling C D 2013 *Chem. Mater.* **25** 3080
[29] Munoz A, de la Calle C, Alonso J A, Botta P M, Pardo V, Baldomir D and Rivas J 2008 *Phys. Rev.* B **78** 054404
[30] Zainullina V M, Leonidov I A and Kozhevnikov V L 2002 *Phys. Solid State* **44** 2063
[31] Stolen S, Bakken E and Mohn C E 2006 *Phys. Chem. Chem. Phys.* **8** 429
[32] Mohn C E, Allan N L, Freeman C L, Ravindran P and Stolen S 2004 *Phys. Chem. Chem. Phys.* **6** 3052
[33] Shein I R, Kozhevnikov V L and Ivanovskii A L 2006 *J. Phys. Chem. Solids* **67** 1436
[34] Lontsi-Fomena M, Villesuzanne A, Doumerc J P, Frayret C and Pouchard M 2008 *Comput. Mater. Sci.* **44** 53
[35] Ricchiardi G, Damin A, Bordiga S, Lamberti C, Spanò G, Rivetti F and Zecchina A 2001 *J. Am. Chem. Soc.* **123** 11409
[36] Bordiga S, Damin A, Bonino F, Ricchiardi G, Zecchina A, Tagliapietra R and Lamberti C 2003 *Phys. Chem. Chem. Phys.* **5** 4390
[37] Eilertsen E A, Giordanino F, Lamberti C, Bordiga S, Damin A, Bonino F, Olsbye U and Lillerud K P 2011 *Chem. Commun.* **47** 11867
[38] Schober H, Tölle A, Renker B, Heid R and Gompf F 1997 *Phys. Rev.* B **56** 5937
[39] Kresse G and Furthmuller J 1996 *Phys. Rev.* B **54** 11169
[40] Parlinski K, Li Z Q and Kawazoe Y 1997 *Phys. Rev. Lett.* **78** 4063
[41] Parlinski K 2010 PHONON Software www.computingformaterials.com *Crakow*
[42] Tobbens D M and Kahlenberg V 2011 *Vib. Spectrosc.* **56** 265
[43] Merrick J P, Moran D and Radom L 2007 *J. Phys. Chem.* A **111** 11683
[44] Aroyo M I, Kirov A, Capillas C, Perez-Mato J M and Wondratschek H 2006 *Acta Crystallogr.* A **62** 115
[45] Kroumova E, Capillas C, Aroyo M I, Perez-Mato J M, Ivantchev S, Madariaga G, Kirov A, Wondratschek H, Stokes H T and Hatch D M 2003 *IOP Conf. Ser.* **173** 383

[46] Kroumova E, Aroyo M I, Perez-Mato J M, Kirov A, Capillas C, Ivantchev S and Wondratschek H 2003 *Phase Transit.* **76** 155
[47] Yu P and Cardona M 2010 Fundamentals of Semiconductors. Physics and Materials Properties (Berlin: Springer)
[48] Wolverson D 2013 in *Characterization of Semiconductor Heterostructures and Nanostructures* vol II, ed C Lamberti and G Agostini (Amsterdam: Elsevier) p 753
[49] Momma K and Izumi F 2008 *J. Appl. Crystallogr.* **41** 653
[50] Brown I D 2002 *The Chemical Bond in Inorganic Chemistry: The Bond Valence Model* (Oxford: Oxford University Press)
[51] Damin A, Bonino F, Bordiga S, Groppo E, Lamberti C and Zecchina A 2006 *ChemPhysChem* **7** 342
[52] Vishnuvarthan M, Paterson A J, Raja R, Piovano A, Bonino F, Gianotti E and Berlier G 2011 *Microporous Mesoporous Mater.* **138** 167
[53] Bonino F, Damin A, Piovano A, Lamberti C, Bordiga S and Zecchina A 2011 *ChemCatChem* **3** 139